JOURNAL OF APPLIED CRYSTALLOGRAPHY

ISSN 1600-5767

Received 27 November 2024
Accepted 19 January 2025

Edited by J. Keckes, Montanuniversität Leoben, Austria

Keywords: DSNet; small-angle scattering; smearing effects; deep learning; desmearing.

Deep-learning-powered desmearing for small-angle scattering

Weigang Zhou,[a] Xiuguo Chen,[a,b]* Jiahao Zhang,[a] Shuo Liu,[a] Dingxuan Deng,[a] Shilong Yang,[a] Zirong Tang[a] and Shiyuan Liu[a,b]

[a]State Key Laboratory of Intelligent Manufacturing Equipment and Technology, Huazhong University of Science and Technology, Wuhan 430074, People's Republic of China, and [b]Optics Valley Laboratory, Wuhan 430074, People's Republic of China. *Correspondence e-mail: xiuguochen@hust.edu.cn

Smearing effects in small-angle scattering (SAS) measurements significantly compromise data analysis, arising from the convolution of theoretical scattering curves with the point spread function of the measurement system. This paper presents a deep-learning-based desmearing network (DSNet) designed to effectively mitigate smearing effects in SAS data. By integrating the processes underlying scattering data smearing, DSNet necessitates only a limited simulation dataset for pre-training. Both simulation and experimental results have demonstrated that DSNet exhibits robust noise resilience and exceptional generalization performance across diverse sample types, and achieves superior desmearing capabilities compared with the classical Lake method and Wiener filter.

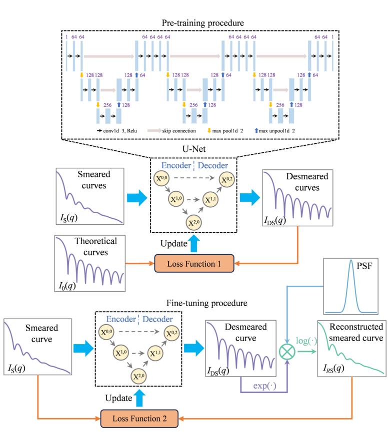

1. Introduction

The small-angle scattering (SAS) technique, including small-angle X-ray scattering (SAXS) and small-angle neutron scattering, has become indispensable for investigating submicrometre structures and morphological features of materials (Orji *et al.*, 2018; Jeffries *et al.*, 2021; Wu *et al.*, 2023*b*). The theoretical scattering intensity distribution is obtained under ideal conditions, which include high-energy point sources and high-resolution detectors. However, practical experimental procedures are susceptible to factors such as the wavelength spread of the monochromator system, finite collimation and the spatial resolution of the detector (Pedersen *et al.*, 1990), leading to deviations in the measured scattering intensity distribution from theoretical expectation. These discrepancies give rise to a smearing effect in the scattering spectra, characterized by diminished peaks and elevated valleys, which ultimately leads to a smoothed scattering intensity distribution. These smearing effects create significant disparities between measured data and theoretical scattering cross-sections, profoundly complicating the data analysis process.

Over the past few decades, researchers have explored various methods for desmearing SAS data. The first approach, proposed by Van Cittert (1931), employed an iterative algorithm and was applied to 2D scattering patterns. Later, Lake (1967) developed another iterative method for 1D scattering curves, which later became a classical desmearing method due to its ability to avoid restrictions on the weight function in both width and height directions (Pilz *et al.*, 1979). Other desmearing methods similarly resolved the data-smearing effects by analysing the underlying mathematical principles of SAS, exemplified by spline interpolation (Taylor & Schmidt, 1967; Schelten & Hossfeld, 1971), deconvolution techniques

(Chen *et al.*, 2016; Hua *et al.*, 2017), Fourier transform (Glatter, 1977; Moore, 1980; Jaksch *et al.*, 2021), the Wiener filter (Le Flanchec *et al.*, 1996) and central moment expansion (Huang *et al.*, 2023).

In recent years, deep learning has undergone rapid advancements, leading to significant improvements across various applications. Among these, addressing different types of image blur has seen considerable progress. Image issues such as motion blur, out-of-focus blur, Gaussian blur and mixed blur have been effectively addressed through innovative deep-learning techniques (Zhang *et al.*, 2022). Within the field of SAS, deep learning has also exhibited remarkable efficacy. This has been evident in several critical applications, including image inpainting, which is employed to fill in gaps within detector images (Chavez *et al.*, 2022). Additionally, deep-learning methods have been utilized for denoising, thereby enhancing the clarity of the data (Zhou *et al.*, 2024), and for filtering diffraction pattern images, which is crucial for analysing complex scattering patterns (Dong *et al.*, 2024). Despite these advancements, to the best of our knowledge, there is no report yet on the desmearing of SAS data using deep learning. This represents a significant gap in the current research landscape, suggesting that further exploration into this area could yield valuable insights and advancements in the field.

In this paper, we have proposed a deep-learning-based desmearing network (DSNet) designed to address the desmearing issue in SAS measurement data. Unlike traditional deep-learning approaches, DSNet requires only a limited amount of simulation data for pre-training, thus eliminating the need for a large number of labelled and experimental datasets. Moreover, by incorporating the smearing process in SAS, DSNet demonstrates excellent generalization performance, effectively mitigating smearing effects across a range of sample structures. When applied to both simulated and experimental data, DSNet exhibits strong noise resistance and achieves superior desmearing capabilities compared with the Lake method and Wiener filter.

2. Methods

2.1. The smearing effect

Numerous studies have been conducted to explore resolution problems in SAS (Ramakrishnan, 1985; Wignall, 1991). Pedersen *et al.* (1990) provided an analytical treatment of the different resolution effects by the resolution function or the point spread function (PSF) $R(q, q')$, where q is the scattering vector magnitude corresponding to the setting of the instrument and q' is the average scattering vector magnitude. The PSF $R(q, q')$ describes the distribution of the radiation with q' contributing to the scattering for the setting q. According to this, the smeared intensity at q is proportional to

$$I_{\rm S}(q) = \int R(q, q') \frac{{\rm d}\sigma(q')}{{\rm d}\Omega} {\rm d}q', \tag{1}$$

where ${\rm d}\sigma(q')/{\rm d}\Omega$ is the theoretical scattering cross-section and $I_{\rm S}(q)$ indicates the smeared scattering curve. For brevity, the experimental scattering curve can be represented as the convolution of a theoretical scattering curve with the instrumental PSF,

$$I_{\rm S}(q) = I_0(q) \otimes {\rm PSF}(q, q'), \tag{2}$$

where $\otimes$ represents the convolution operation and $I_0(q)$ denotes the theoretical scattering curve. In an ideal high-resolution scenario, the PSF can be approximated as a delta function $\delta(x)$, resulting in $I_{\rm S}(q)$ being equal to $I_0(q)$. However, in practical applications, the PSF typically exhibits broadening, leading to deviations of the smeared scattering curve from the theoretical scattering curve; this phenomenon is referred to as the smearing effect. In the frequency domain, the smearing effect can be expressed as follows:

$$\mathcal{F}\big\{I_{\rm S}(q)\big\} = \mathcal{F}\big\{I_0(q)\big\}\ \mathcal{F}\big\{{\rm PSF}(q, q')\big\}, \tag{3}$$

where $\mathcal{F}\{\cdot\}$ represents the Fourier transform. In SAS, the PSF is typically modelled as a Gaussian function (Pedersen *et al.*, 1990) and its Fourier transform, $\mathcal{F}\{{\rm PSF}(q, q')\}$, retains a Gaussian form. This serves as a low-pass filter, attenuating high-frequency components in the theoretical scattering curves. The loss of these high-frequency details limits the desmearing process, preventing full recovery of the fine features of the original scattering curve and leading to ill-posed deconvolution problems. Specifically, the absence of high-frequency information makes deconvolution unstable, resulting in a non-unique solution that is highly sensitive to noise.

2.2. Principle of DSNet

Fig. 1 presents the architecture of DSNet; our desmearing method contains two procedures: a pre-training procedure [Fig. 1(*a*)] and a fine-tuning procedure [Fig. 1(*b*)]. For the pre-training procedure, the inputs are smeared curves [$I_{\rm S}(q)$] which are logarithmically transformed to improve data visualization and facilitate more effective analysis, and the outputs are the corresponding desmeared curves [$I_{\rm DS}(q)$]. The pre-training procedure is updated by minimizing the mean squared error (MSE) between the desmeared curves $I_{\rm DS}(q)$ and the theoretical curves $I_0(q)$, as follows:

$${\rm MSE} = \frac{1}{N}\sum_{i=1}^{N}\big[I_{\rm DS}(q_i) - I_0(q_i)\big]^2, \tag{4}$$

where N represents the total number of data points for q.

For the fine-tuning procedure, the inputs include the logarithmically transformed smeared curve $I_{\rm S}(q)$ and the system PSF; the output is the corresponding desmeared curve $I_{\rm DS}(q)$. After exponentiation, the desmeared curve is convolved with the PSF. Taking the logarithm of the convolution result yields the reconstructed smeared curve $I_{\rm RS}(q)$. The fine-tuning procedure is updated by comparing the reconstructed smeared curve with the original smeared curve until they align to an acceptable degree. This indicates that the output of the network represents the desmeared result of the original smeared curve within the given experimental condition. Here, we also use the MSE as the loss function to evaluate the difference between the reconstructed smeared curve $I_{\rm RS}(q)$ and the input smeared curve $I_{\rm S}(q)$ as follows:

$$\mathrm{MSE} = \frac{1}{N}\sum_{i=1}^{N}\left[I_{\rm RS}(q_i) - I_{\rm S}(q_i)\right]^2. \tag{5}$$

As the smeared scattering curve and the desmeared results share the same dimensions, the same U-Net is employed in the pre-training and fine-tuning procedures to fully exploit the data features of the scattering curves. To extract deeper curve features and enhance the expressiveness and robustness of the network, the U-Net architecture [Fig. 1(*a*)] used in DSNet is composed of three U-Net-type structures. The input smeared curve $I_{\rm S}(q) \in \mathbb{R}^{M\times N}$ (the initial channel $M = 1$, and $N = 501$ is the number of data points for the smeared curve) is fed into the encoder. Following convolution and max-pooling operations, the data are passed into the decoder, where they undergo max-unpooling and additional convolution steps, ultimately yielding the output desmeared curve $I_{\rm DS}(q) \in \mathbb{R}^{M\times N}$.

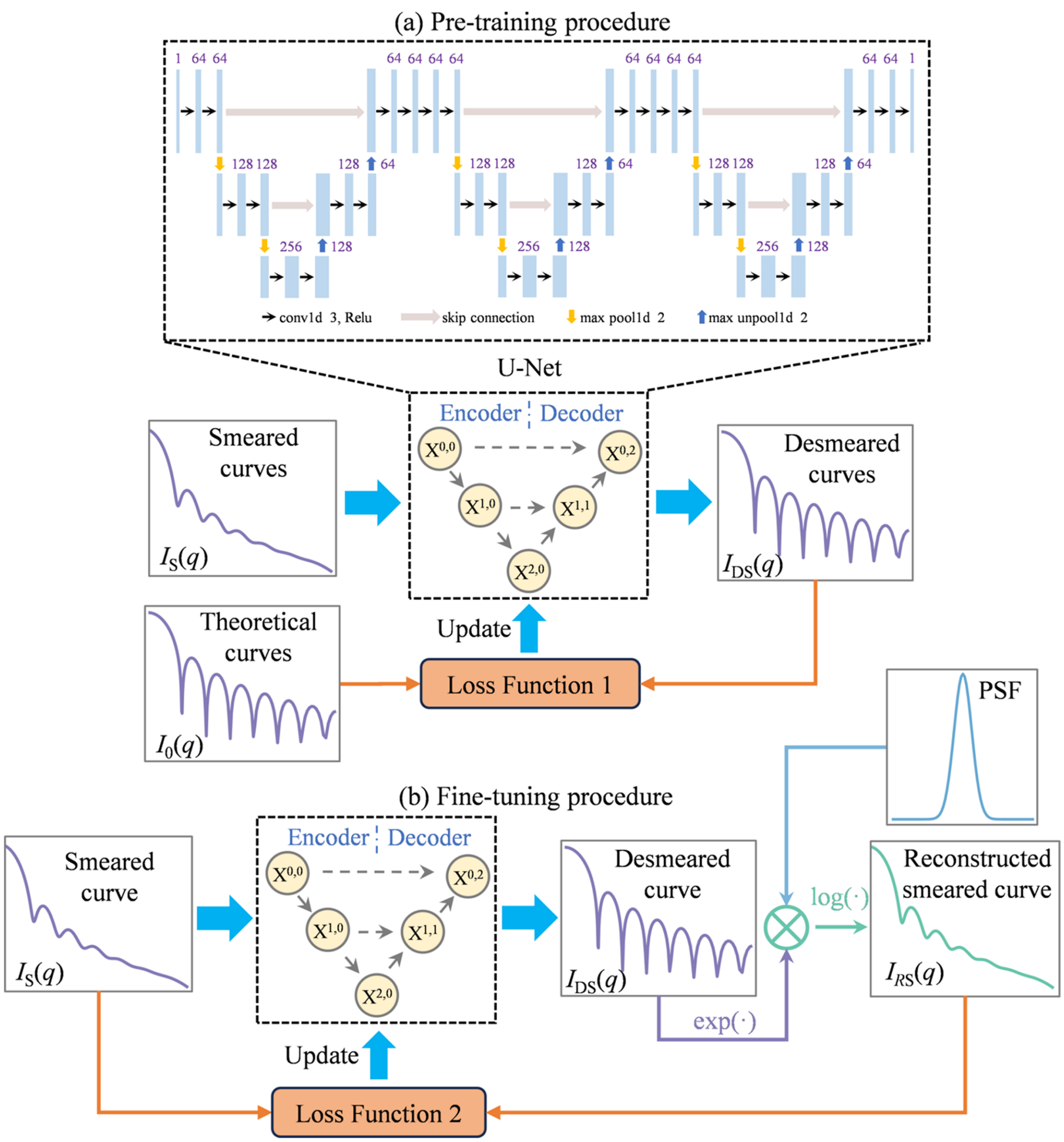

Figure 1
Overview of DSNet. The proposed desmearing method contains two procedures: (*a*) pre-training procedure and (*b*) fine-tuning procedure. During the pre-training procedure, the inputs are logarithmically transformed smeared curves $[I_{\rm S}(q)]$ and the outputs are the corresponding desmeared curves $[I_{\rm DS}(q)]$. The pre-training procedure is updated by comparing the desmeared curves with the theoretical curves. During the fine-tuning procedure, the inputs are the logarithmically transformed smeared curve $[I_{\rm S}(q)]$ and the system PSF; the output is the corresponding desmeared curve $[I_{\rm DS}(q)]$. After exponentiation, the desmeared curve is convolved with the PSF. Taking the logarithm of the convolution result yields the reconstructed smeared curve $I_{\rm RS}(q)$. The fine-tuning procedure is updated by comparing the reconstructed smeared curve with the original smeared curve. The upper presents the architecture of the used concatenated U-Net. Three U-Net-type structures connected together are employed to extract deeper curve features and enhance the expressiveness and robustness of the network. The U-Net architectures used in the pre-training and fine-tuning are the same.

2.3. Network pre-training and fine-tuning

To avoid the ill-posed problems of deconvolution discussed in Section 2.1, we first employ a pre-training procedure using simulated data generated by the *Sasview* software (https://www.sasview.org/). Specifically, we generate 100 theoretical scattering curves for spheres with diameters ranging from 1 to 100 Å and select a Gaussian function with a standard deviation of $\sigma = 2 \times 10^{-2}$ nm^{-1} as the system PSF. The smeared curves are obtained by convolving the theoretical curves with the prescribed PSF in the absence of noise. We divide these simulated data into a training set and a test set in a 9:1 ratio. DSNet is pre-trained using the MSE loss from equation (4). We utilize the Adam optimizer (Diederik & Jimmy, 2014) with an initial learning rate of 0.0001 and a batch size of 90, training the network for 500 epochs. During the pre-training, we compute the accuracy on the test set after each epoch; if the current accuracy exceeds the previously recorded highest accuracy, we save the parameters of the network.

After pre-training on the simulated data, DSNet is fine-tuned using experimental SAS data exhibiting smearing effects. The saved network parameters during pre-training serve as the starting point for fine-tuning on experimental data, significantly improving the performance and reducing training time. This fine-tuning process enables the network to retain essential features learned during pre-training while adapting to the specific nuances of the experimental data. For fine-tuning, the Adam optimizer is employed with a reduced learning rate of 0.00001 to facilitate more precise adjustments. The loss function is defined by equation (5) and the network is fine-tuned for an additional 500 epochs.

The pre-training procedure is performed on simulated data, where theoretical scattering curves guide DSNet in learning and understanding the physical features of scattering, rather than simply serving as a mathematical parameter initialization. This step provides a strong foundation for the subsequent fine-tuning procedure. By relying on the scattering features it has learned, DSNet can handle real data more effectively, improving desmearing accuracy without solely depending on data-driven matching. Compared with traditional random initialization, pre-training allows the network to begin with a more robust foundation, enabling it to focus on capturing fine details and making precise adjustments, while avoiding overfitting, reducing sensitivity to noise and accelerating convergence. During the fine-tuning procedure, the system PSF is used to simulate the smearing process of the actual scattering curves, further guiding the network's learning and enhancing its ability to address system-induced smearing, thus improving the robustness and generalization capacity of DSNet. The entire process was conducted on a computer workstation with a central processing unit (Intel Xeon E5-2643v4 at 3.4 GHz), 128 GB of RAM and three graphics processing units (GeForce RTX 2080 Ti).

3. Test with synthetic data

To assess the desmearing capabilities of DSNet on smeared curves, we employ the *Sasview* software to generate theoretical scattering curves as the ground truth and apply a Gaussian function with $\sigma = 4 \times 10^{-2}$ nm^{-1} as the PSF. The smeared curves are produced by convolving the theoretical scattering curves with the PSF. In our simulations, we first evaluate the robustness of DSNet to noise by introducing varying levels of noise to the scattering spectra of a sphere. To further test its generalization performance, we use scattering spectra from different samples, including a cylinder, a simple cubic lattice and polydisperse spheres. We also employ a PSF with a standard deviation different from that used in pre-training, applying this PSF throughout the simulations. For comparison, we evaluate the results obtained from DSNet against those from the Lake method and Wiener filter. Note that due to the sensitivity of the Lake method to noise, a smoothed version (Vad & Sager, 2011) is used below.

3.1. Noise robustness

In practical SAS measurements, noise is a significant factor that induces fluctuations in the scattering curves. As the noise

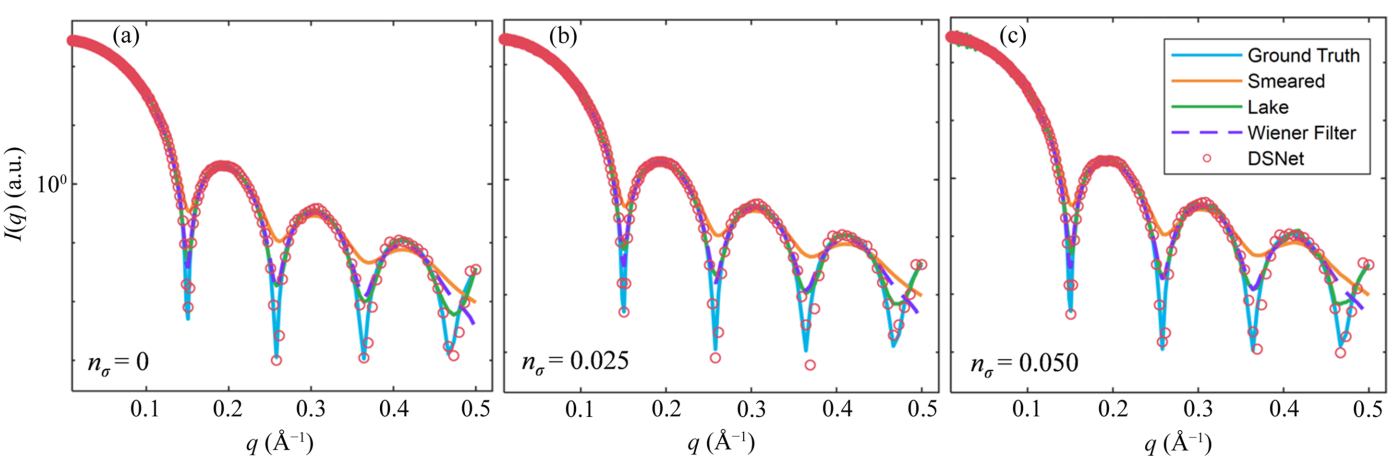

Figure 2
Desmearing results with different levels of noise. The ground truth $I(q)$ (blue curve), smeared $I(q)$ (orange curve), Lake desmearing $I(q)$ (green curve), Wiener filter desmearing $I(q)$ (purple dashed curve) and DSNet desmearing $I(q)$ (red circles) using different levels of noise (n_σ), with (*a*) $n_\sigma = 0$, (*b*) $n_\sigma = 0.025$ and (*c*) $n_\sigma = 0.050$. The sample is a sphere with a uniform scattering length density and a radius of 30 Å.

Table 1
Performance comparison of different desmearing methods with varying noise levels.

The values in the table represent the MSE between the theoretical scattering curves and the desmeared curves. The sample is a sphere with a uniform scattering length density and a radius of 30 Å.

Desmearing methods	Lake method	Wiener filter	DSNet
$n_\sigma = 0$	0.0495	0.0928	0.0178
$n_\sigma = 0.025$	0.0527	0.0916	0.0284
$n_\sigma = 0.050$	0.0588	0.0903	0.0216

level increases, the signal-to-noise ratio of the scattering curves decreases markedly, especially in the high-q region. We utilize a noise model (Vad & Sager, 2011) to introduce noise to the simulated smeared scattering curve $I_S(q)$ of a sphere with a radius of 30 Å by

$$\sigma(q) = \pm n_\sigma p I_S(q), \tag{6}$$

where n_σ represents the maximum relative deviation and is assigned values of 0.025 or 0.050, and p is a random number indicating the proportion of $n_\sigma I_S(q)$ to be randomly added to or subtracted from the smeared intensity value $I_S(q)$.

As shown in Fig. 2(*a*), in the absence of noise, the Lake method, Wiener filter and DSNet produce relatively smooth desmearing results. However, regarding recovery accuracy, both the Lake method and the Wiener filter only partially reconstruct the original curve's features, whereas DSNet nearly fully restores all characteristics, particularly at the sharp minima. Once noise is introduced, as shown in Figs. 2(*b*) and 2(*c*), the desmearing results of the Lake method exhibit increasing fluctuations as noise levels rise, despite the smoothing applied. In contrast, the Wiener filter and DSNet effectively mitigate the impact of noise at lower levels. Even as noise increases, the Wiener filter remains relatively stable. However, the Wiener filter can only partially recover the features of the scattering curve. Although DSNet exhibits only minor fluctuations in the high-q region, the low-q region and the peak characteristics of the original scattering curve are largely preserved, demonstrating DSNet's strong robustness against noise. The MSE between the theoretical scattering curves and the desmeared curves, as presented in Table 1, indicates that both the Wiener filter and DSNet exhibit greater stability against noise, with DSNet demonstrating the best desmearing performance.

The superior performance of DSNet in handling noise can be attributed to its deep-learning architecture, which allows it to better capture and generalize the underlying patterns in the scattering curves. In contrast to the Lake method, which relies on iterative deconvolution, DSNet learns the complex relationships between smeared and desmeared data through its pre-training and fine-tuning procedures. This capability allows DSNet to distinguish between genuine scattering features and noise. For the Wiener filter, the introduction of the power spectral densities of the signal and noise can help suppress the impact of noise to some extent.

3.2. Generalization

A critical aspect of any deep-learning method is its ability to generalize effectively. To assess the generalization performance of DSNet, we evaluate samples that were not seen during pre-training, including a right circular cylinder with uniform scattering length density, a simple cubic lattice with paracrystalline distortion and polydisperse spheres. These structures differ significantly from the pre-training data, facilitating a comprehensive evaluation of the adaptability of DSNet to previously unseen scattering spectra.

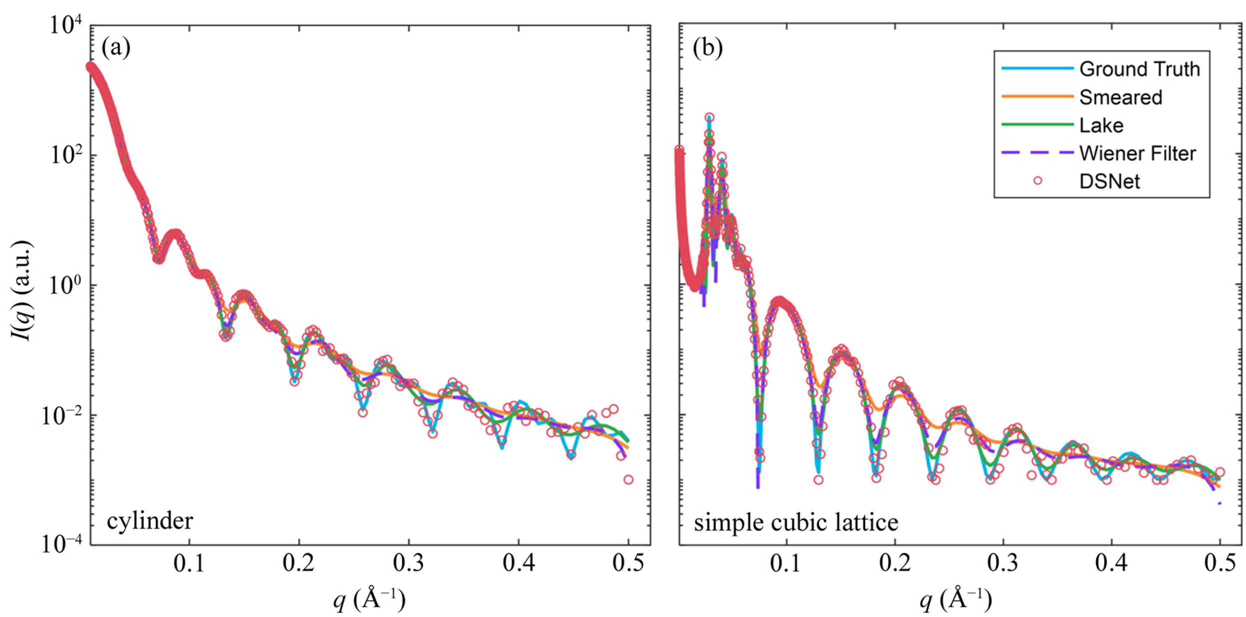

Figure 3
Desmearing results of different sample types. The ground truth $I(q)$ (blue curve), smeared $I(q)$ (orange curve), Lake desmearing $I(q)$ (green curve), Wiener filter desmearing $I(q)$ (purple dashed curve) and DSNet desmearing $I(q)$ (red circles) using different sample types: (*a*) right circular cylinder with a uniform scattering length density and (*b*) simple cubic lattice with paracrystalline distortion.

Table 2
Performance comparison of different desmearing methods using different sample types.

The values in the table represent the MSE between the theoretical scattering curves and the desmeared curves.

Desmearing methods	Lake method	Wiener filter	DSNet (with fine-tuning)	DSNet (without fine-tuning)
Cylinder	0.0185	0.0362	0.0155	0.0484
Simple cubic lattice	0.0866	0.1699	0.0360	0.2388

As illustrated in Fig. 3(*a*), the scattering curve of the cylinder differs significantly from that of the sphere, displaying less variation between peaks and valleys and exhibiting a more rugged appearance. The desmearing results obtained using the Lake method are consistent with those presented in Section 3.1, wherein only partial features of the curve are restored. This method struggles with sharp minima and is unable to recover certain smaller peak features. The desmearing result of the Wiener filter is similar to that of the Lake method, with some peak features lost in the high-q region. In contrast, DSNet effectively addresses these challenges, nearly fully recovering the original information of the scattering curve. When examining the simple cubic lattice sample, which presents a more complex scattering curve as shown in Fig. 3(*b*), the Lake method exhibits oscillations in the low-q region, causing the desmeared results to deviate significantly from the theoretical scattering curves. The performance of the Wiener method on this sample is inferior to that of the Lake method. In addition to losing peak features in the high-q region, significant oscillations appear in the low-q region, disrupting the desmeared scattering curve. Conversely, DSNet does not encounter this issue, demonstrating its robust generalization to handle complex scattering curves.

Table 2 presents the MSE between the desmeared curves and the theoretical scattering curves for different methods. DSNet demonstrates the best performance in desmearing for both sample types, followed by the Lake method. The Wiener filter exhibits significantly higher MSE, particularly for the simple cubic lattice sample, due to the oscillations observed in the results. Since the scattering curves in this test differ significantly from those used during pre-training, it is interesting to evaluate the performance of the pre-trained model without any fine-tuning. As shown in the last column of Table 2, the results of DSNet without fine-tuning demonstrate poor performance for both the cylinder and the simple cubic lattice, which underscores the importance of the fine-tuning process.

These results confirm that DSNet demonstrates excellent generalization performance, effectively desmearing SAS data from different sample structures with minimal accuracy loss. However, note that in both Figs. 3(*a*) and 3(*b*) the desmeared curves produced by DSNet exhibit minor fluctuations. This may be attributed to the significant differences between the scattering curve features and those learned by the network during pre-training. Therefore, incorporating a greater variety of sample structures and amount of data during pre-training may enable the network to learn additional feature information, potentially enhancing desmearing capabilities.

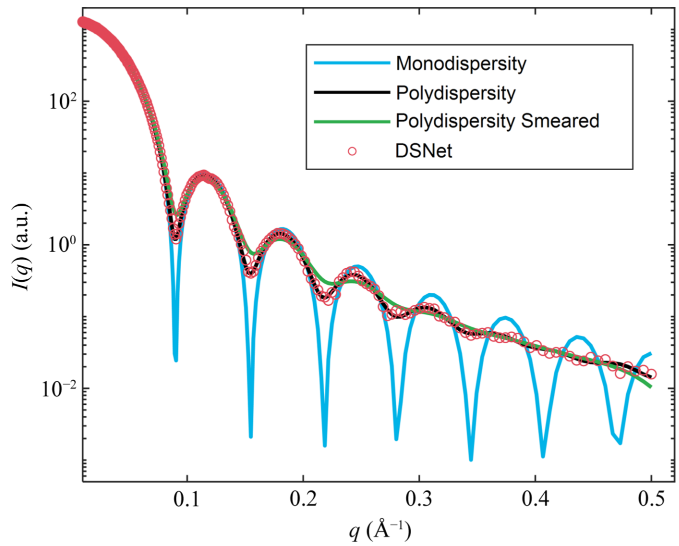

Figure 4
Desmearing results of polydisperse spheres. The blue curve represents the scattering curve of a monodisperse sphere with a radius of 50 Å, the black curve represents the scattering curve of the corresponding polydisperse spheres with a log-normal size distribution, the green curve represents the effect of system smearing on the polydisperse spheres and the red circles represent the desmeared scattering curve obtained using DSNet.

In SAS, nanoparticle size polydispersity can distort the peaks and valleys of scattering curves (Wu *et al.*, 2023*a*). As shown in Fig. 4, we used the *Sasview* software to generate the scattering curves for both a monodisperse sphere with a radius of 50 Å and the corresponding polydisperse spheres with a log-normal size distribution. The scattering curve of the polydisperse spheres is then convolved with a Gaussian PSF of $\sigma = 4 \times 10^{-2}\ \mathrm{nm}^{-1}$ to obtain the smeared scattering curve. Subsequently, we apply DSNet to desmear this curve. The results demonstrate that DSNet effectively corrects the smearing induced by the system PSF, restoring the minima in the low-q region of the polydisperse spheres while preserving the high-q region without introducing artificial minima.

4. Experimental results

While the simulation results provide a solid foundation, practical applications introduce complexities such as noise and variations in sample characteristics that must be addressed. To assess the robustness of DSNet and its generalization performance across different sample structures and instruments, we selected two samples and two instruments for experimentation. Specifically, a silver behenate (AgBeh) powder sample was tested using the Xeuss 3.0 UHR (Xenocs, France) SAXS instrument, equipped with a Cu $K\alpha$ X-ray source that emits X-rays with a 0.154 nm wavelength. A 1D grating structure sample was tested with an in-house laboratory SAXS (Lab-SAXS) instrument, equipped with an In $K\alpha$ X-ray source (Excillum, Sweden) emitting 0.051 nm X-rays. During the experiment, the slit configuration is first adjusted. Then, without the sample and beamstop, a 1 s exposure is performed to capture the 2D direct beam profile, which is integrated to

Table 3
Exposure times for different slit sizes (two slits with square cross-sections).

Slit configuration	(1)	(2)	(3)	(4)
Slit size (mm × mm)†	4.0 × 2.5	2.5 × 1.4	1.6 × 0.9	0.8 × 0.5
Photon flux (counts s^{-1})	1×10^8	0.6×10^8	0.24×10^8	0.024×10^8
Exposure time (s)	60	100	250	2500

† The slit size $A \times B$ means that the side lengths of the first and second square slits are A and B, respectively.

Table 4
MSE comparison of experimental and desmeared scattering curves for different slit configurations with slit configuration (4).

Slit configuration	(1)	(2)	(3)
Experimental curve	278.2676	134.3475	50.4785
Desmeared curve	28.5563	26.2302	25.2406

obtain the 1D PSF of the instrument under the slit configuration. Finally, the beamstop and sample are placed, and exposure measurements are conducted.

4.1. AgBeh powder

The AgBeh powder sample was measured under different slit sizes. To maintain consistent scattering intensity across configurations, the exposure time for each slit setting was calculated on the basis of the photon flux, as detailed in Table 3. Since the AgBeh powder was tested on the same instrument, the degree of curve recovery after desmearing should be the same.

For each slit configuration, we first measured the direct beam profile in a vacuum environment to obtain the 1D PSF. Next, the AgBeh powder was exposed and 2D scattering patterns were collected. These patterns were azimuthally averaged to produce 1D scattering curves. The experimental results for the four slit configurations are shown in Fig. 5(*a*). As the slit opening increases, the peak height of the scattering curve decreases, while its width broadens, reflecting a more pronounced smearing effect. Then we input the 1D scattering curves and corresponding PSFs into DSNet, loaded the pre-trained network parameters, and performed the fine-tuning procedure to desmear. The desmearing results, displayed in Fig. 5(*b*), show that, despite some minor fluctuations, the desmeared curves remain largely consistent across different slit configurations. We select the curves of slit configuration (4) as the reference and calculated the MSE between the experimental and desmeared scattering curves for the other three configurations and the curves for slit configuration (4). As shown in Table 4, once the slit size decreases, the MSE between the experimental curve and the reference configuration's experimental curve decreases, indicating a reduction in the smearing effect. After desmearing with DSNet, the MSE between the desmeared curve and the reference configuration's desmeared curve shows minimal difference, demonstrating the consistency of the desmearing results.

4.2. 1D grating structure

The 1D grating structure consists of trapezoidal nanostructures with a periodicity of 125 nm. Due to the weak scattering signal from this sample, a higher-energy X-ray source was employed. The experimental setup included 1.2 mm × 0.5 mm slit sizes and a 7500 s exposure time. Firstly, the direct beam was measured to obtain the 1D PSF. The experiment was then performed on the 1D grating structure sample. We also measured the 1D grating structure at the BL16B beamline of the Shanghai Synchrotron Radiation Facility (SSRF) with an exposure time of 15 s, using it as a reference, as shown in Fig. 6(*a*). Fig. 6(*b*) shows the SAXS pattern using Lab-SAXS, which indicates that the long exposure time resulted in significant noise interference, rendering the last few scattering orders nearly indistinguishable. By integrating the scattering signals within the red rectangles in Figs. 6(*a*) and 6(*b*), the 1D scattering curves in Fig. 6(*c*) were derived. Similarly to the 2D pattern, when $q > 0.4$ nm^{-1}, the

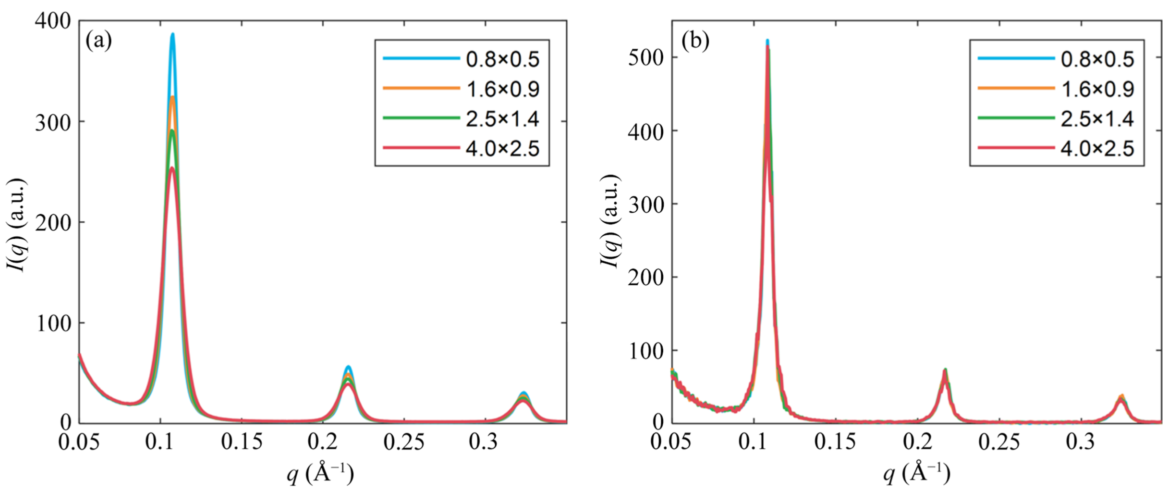

Figure 5
Experimental and desmearing results of AgBeh powder. (*a*) Experimental SAXS data of AgBeh powder with different slit sizes. (*b*) Desmeared curves of the experimental data of AgBeh powder in (*a*) using DSNet.

Table 5
Performance comparison of different desmearing methods for the 1D grating structure.

The values represent the MSE between the SSRF scattering curves and the desmeared curves.

Desmearing methods	Lake method	Wiener filter	DSNet
MSE	3.0769	3.3592	2.8517

noise of the scattering curve measured by Lab-SAXS becomes comparable to the scattering intensity, significantly degrading the signal quality.

Notably, the 1D curve obtained from Lab-SAXS contains only 100 data points, which is inconsistent with the dataset used during pre-training. To align the scattering curve for processing in DSNet, the tail of the 1D scattering curve must be extended with a constant value until it reaches 501 data points. This allows the scattering curve, along with the PSF, to be input into DSNet for fine-tuning. As shown in Fig. 6(*c*), the Wiener filter primarily smooths the scattering curve, partially recovering the valley features. The Lake method exhibits similar results to the Wiener filter, but with larger disturbances. In contrast, DSNet restores sharper peaks, bringing the curve closer to the scattering data measured at SSRF (as shown in Table 5).

The experiments on AgBeh powder and the 1D grating structure thus demonstrated the efficacy of DSNet in mitigating the smearing effect in SAS measurement data. The results highlight the robustness of DSNet to noise and its strong generalization performance. Note that for the 1D grating structure, while our desmearing result is promising, some differences persist when compared with the SSRF measurement. This discrepancy stems from the fact that our current approach considers only the PSF induced by the structure of the instrument. In practice, other factors, such as the wavelength distribution of the light source and the spatial resolution of the detector, also contribute to the overall smearing effect. Addressing these additional factors will be a key focus of future improvements to DSNet.

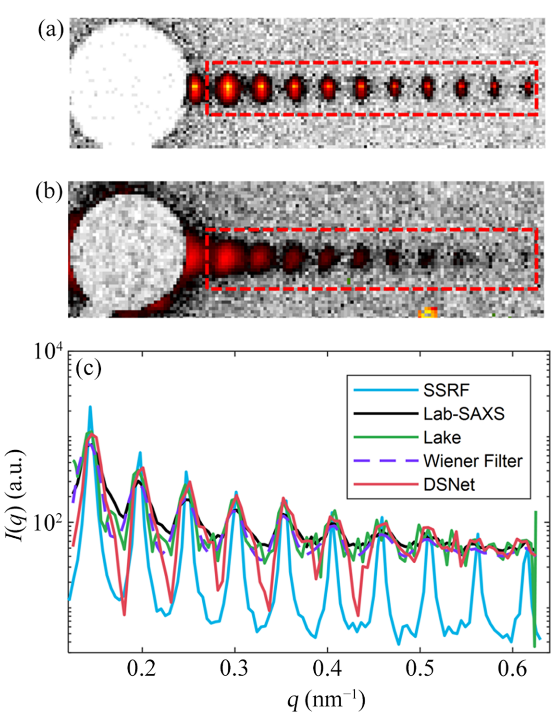

Figure 6
Experimental and desmearing results of the 1D grating structure. (*a*) Experimental 2D SAXS pattern using the SSRF SAXS instrument. (*b*) Experimental 2D SAXS pattern using the Lab-SAXS instrument. (*c*) 1D SAXS curve: SSRF $I(q)$ (blue curve), Lab-SAXS $I(q)$ (black curve), Lake desmearing $I(q)$ (green curve), Wiener filter desmearing $I(q)$ (purple dashed curve) and DSNet desmearing $I(q)$ (red curve).

5. Discussion

Although DSNet has demonstrated promising efficacy in mitigating the smearing effect in SAS measurements, it is essential to recognize the limitations of this approach.

Firstly, the performance of DSNet is not equally effective across all levels of smearing. As shown in Fig. 7, when a Gaussian PSF with $\sigma = 8 \times 10^{-2}\ \mathrm{nm}^{-1}$ and noise level $n_\sigma = 0.050$ are applied to a 30 Å sphere, the smearing is too severe, leading to peak overlap that DSNet cannot adequately resolve.

Secondly, for a dataset of 100 curves, the pre-training time for DSNet is approximately 25 s. During the fine-tuning procedure, each iteration takes about 0.023 s. Reliable results are typically achieved in fewer than 500 iterations, completing the desmearing process in approximately 12 s. While the fine-tuning time is acceptable in our current experiments, further optimization is possible. Potential improvements include increasing the diversity and quantity of the training set, simplifying model parameters, or fixing certain parameters during fine-tuning. These enhancements could enable integration of the method for online analysis of SAS data in future work.

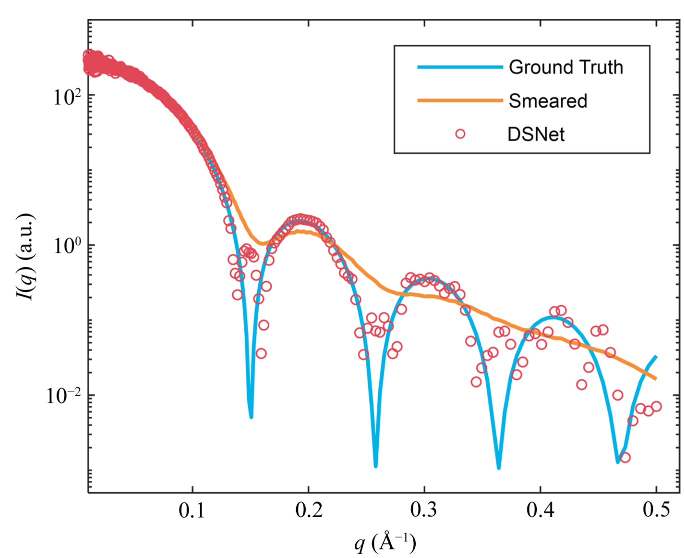

Figure 7
Desmearing results of the sphere with an extremely severe smearing effect. The sample is a sphere with a uniform scattering length density and a radius of 30 Å.

Thirdly, although the current method enables rapid generation of a desmeared scattering curve, it sacrifices uncertainty information, which may impact subsequent analyses that depend on precise error estimation. With the ongoing advancement of deep learning, networks designed for uncertainty analysis have also gained attention. For instance, the Bayesian convolutional neural network based framework (Xue *et al.*, 2019) effectively addresses phase prediction and uncertainty assessment during the imaging process, offering a promising direction for future improvements in our work.

Finally, our current method still requires a system PSF as the input for the desmearing process. However, the determination of the PSF involves considering various factors, which could impact the desmearing results. In future work, we will explore a blind desmearing approach for SAS data that does not rely on the PSF.

6. Conclusions

We have presented DSNet, the first deep-learning-based desmearing method specifically designed for SAS measurements. DSNet effectively integrates the processes associated with the smearing of theoretical scattering spectra, minimizing data requirements during pre-training prior to the fine-tuning procedure. Through simulations, we have validated the efficacy of DSNet in mitigating smearing effects. Moreover, our method can be applied across different instruments and samples without necessitating retraining. Both simulation and experimental results demonstrate that DSNet achieves superior desmearing capabilities, enhanced noise robustness and excellent generalization performance, significantly outperforming the classical Lake method and Wiener filter. Though DSNet yields promising results, some minor oscillations were observed in the desmeared curves, likely due to differences between the features of the pre-training data and those of the experimental samples. Incorporating a wider variety of sample structures during pre-training and refining the network's loss function may lead to improved desmearing results. Future research will focus on further exploring the application of deep-learning techniques in SAS desmearing, aiming to reduce reliance on pre-training while enhancing the smoothness and accuracy of desmearing results.

Acknowledgements

The authors appreciate the kind help of Professor Fenggang Bian and Professor Chunming Yang from SSRF.

Data availability

The pre-training and the fine-tuning data for DSNet can be obtained from the author on request. The original code of DSNet is accessible at https://github.com/xiuguochen/DSNet.

Funding information

This work was funded by the National Key Research and Development Plan of China (grant No. 2022YFF0709104), the National Natural Science Foundation of China (grant Nos. 52022034, 62175075, 52130504), and the Innovation Project of Optics Valley Laboratory (grant No. OVL2023PY003).

References

Chavez, T., Roberts, E. J., Zwart, P. H. & Hexemer, A. (2022). *J. Appl. Cryst.* **55**, 1277–1288.
Chen, R., Yi, Z., Liu, J., Liu, Z. & Men, Y. (2016). *Chin. J. Polym. Sci.* **34**, 505–512.
Diederik, P. K. & Jimmy, L. B. (2014). *arXiv*, 1412.6980.115.
Dong, J., Yin, Z., Kreitler, D., Bernstein, H. J. & Jakoncic, J. (2024). *J. Appl. Cryst.* **57**, 670–680.
Glatter, O. (1977). *J. Appl. Cryst.* **10**, 415–421.
Hua, W. Q., Wang, Y. Z., Zhou, P., Hu, T., Li, X., Bian, F. & Wang, J. (2017). *Chin. Phys. C*, **41**, 048001.
Huang, G.-R., Tung, C.-H., Chen, M.-Z., Porcar, L., Shinohara, Y., Wildgruber, C. U., Do, C. & Chen, W.-R. (2023). *J. Appl. Cryst.* **56**, 1537–1543.
Jaksch, S., Pipich, V. & Frielinghaus, H. (2021). *J. Appl. Cryst.* **54**, 1580–1593.
Jeffries, C. M., Ilavsky, J., Martel, A., Hinrichs, S., Meyer, A., Pedersen, J. S., Sokolova, A. V. & Svergun, D. I. (2021). *Nat. Rev. Methods Primers*, **1**, 70.
Lake, J. A. (1967). *Acta Cryst.* **23**, 191–194.
Le Flanchec, V., Gazeau, D., Taboury, J. & Zemb, Th. (1996). *J. Appl. Cryst.* **29**, 110–117.
Moore, P. B. (1980). *J. Appl. Cryst.* **13**, 168–175.
Orji, N. G., Badaroglu, M., Barnes, B. M., Beitia, C., Bunday, B. D., Celano, U., Kline, R. J., Neisser, M., Obeng, Y. & Vladar, A. E. (2018). *Nat. Electron.* **1**, 532–547.
Pedersen, J. S., Posselt, D. & Mortensen, K. (1990). *J. Appl. Cryst.* **23**, 321–333.
Pilz, I., Glatter, O. & Kratky, O. (1979). *Methods Enzymol.* **61**, 148–249.
Ramakrishnan, V. (1985). *J. Appl. Cryst.* **18**, 42–46.
Schelten, J. & Hossfeld, F. (1971). *J. Appl. Cryst.* **4**, 210–223.
Taylor, T. R. & Schmidt, P. W. (1967). *Acta Phys. Austr.* **25**, 293–296.
Vad, T. & Sager, W. F. C. (2011). *J. Appl. Cryst.* **44**, 32–42.
Van Cittert, V. P. H. (1931). *Z. Phys.* **69**, 298–308.
Wignall, G. D. (1991). *J. Appl. Cryst.* **24**, 479–484.
Wu, S., Zuo, X. & Sun, Y. (2023*a*). *J. Appl. Cryst.* **56**, 1739–1750.
Wu, W. L., Kline, R. J., Jones, R. L., *et al.* (2023*b*). *J. Micro/Nanopattern. Mats. Metro.* **22**, 031206.
Xue, Y., Cheng, S., Li, Y. & Tian, L. (2019). *Optica*, **6**, 618–629.
Zhang, K., Ren, W., Luo, W., Lai, W., Stenger, B., Yang, M. & Li, H. (2022). *Int. J. Comput. Vis.* **130**, 2103–2130.
Zhou, Z., Li, C., Fan, L., Dong, Z., Wang, W., Liu, C., Zhang, B., Liu, X., Zhang, K., Wang, L., Zhang, Y. & Dong, Y. (2024). *J. Appl. Cryst.* **57**, 741–754.